

This manuscript has been authored in part by UT-Battelle, LLC, under contract DE-AC05-00OR22725 with the US Department of Energy (DOE). The US government retains and the publisher, by accepting the article for publication, acknowledges that the US government retains a nonexclusive, paid-up, irrevocable, worldwide license to publish or reproduce the published form of this manuscript, or allow others to do so, for US government purposes. DOE will provide public access to these results of federally sponsored research in accordance with the DOE Public Access Plan (<http://energy.gov/downloads/doe-public-access-plan>).

# High oxygen pressure floating zone growth and crystal structure of the layered nickelates $R_4Ni_3O_{10}$ (R=La, Pr)

Junjie Zhang,<sup>1,2,\*</sup> Hong Zheng,<sup>1</sup> Yu-Sheng Chen,<sup>3</sup> Yang Ren,<sup>4</sup> Masao Yonemura,<sup>5,6</sup> Ashfia Huq,<sup>7</sup> and J. F. Mitchell<sup>1</sup>

<sup>1</sup>Materials Science Division, Argonne National Laboratory, Argonne, IL 60439, United States

<sup>2</sup>Materials Science and Technology Division, Oak Ridge National Laboratory, Oak Ridge, TN 37831, United States

<sup>3</sup>ChemMatCARS, The University of Chicago, Argonne, IL 60439, United States

<sup>4</sup>X-ray Science Division, Advanced Photon Source, Argonne National Laboratory, Argonne, IL 60439, United States

<sup>5</sup>Institute of Materials Structure Science, High Energy Accelerator Research Organization, 1-1 Oho, Tsukuba, Ibaraki 305-0801, Japan

<sup>6</sup>Sokendai (The Graduate University for Advanced Studies), Shirakata 203-1, Tokai, Naka 319-1106, Japan

<sup>7</sup>Neutron Scattering Science Directorate, Oak Ridge National Laboratory, Oak Ridge, Tennessee 37831, United States

**ABSTRACT:** Millimeter-sized single crystals of the Ruddlesden-Popper trilayer nickelates  $R_4Ni_3O_{10}$  (R=La, Pr) were successfully grown under high oxygen pressure ( $pO_2$ ) of 20 bar for  $La_4Ni_3O_{10}$  and 140 bar for  $Pr_4Ni_3O_{10}$ , using an optical-image floating zone furnace. Combining synchrotron x-ray, neutron powder diffraction and x-ray single crystal diffraction, the as-grown  $La_4Ni_3O_{10}$  was found to crystallize in the  $Bmab$  space group with  $a=5.4163(13)$  Å,  $b=5.4687(12)$  Å,  $c=27.960(6)$  Å, or in  $P2_1/a$  with  $a=5.4268(2)$  Å,  $b=5.4750(2)$  Å,  $c=27.9807(11)$  Å,  $\beta=90.116(1)^\circ$ , or a mixture of them, depending on the postgrowth cooling conditions.  $Bmab$   $La_4Ni_3O_{10}$  was found to transform to  $P2_1/a$  when annealed under flowing oxygen, implying the monoclinic phase has lower free energy. The as-grown  $Pr_4Ni_3O_{10}$  belongs to  $P2_1/a$  with  $a=5.3792(1)$  Å,  $b=5.4685(1)$  Å,  $c=27.5543(6)$  Å, and  $\beta=90.419(2)^\circ$ , and undergoes a metal-to-metal transitions (MMT) at 157.6 K. For  $La_4Ni_3O_{10}$ , the MMT depends on the lattice symmetry: 147.5 K for  $Bmab$  vs. 138.6 K for  $P2_1/a$ . The 147.5 K transition was not reported previously. The lattice parameters obtained from Rietveld refinements on both x-ray and neutron powder diffraction data, in particular the middle axis  $b$ , exhibit an anomaly at the MMTs, demonstrating lattice response to electronic transitions. The MMT temperatures correlate with the in-plane and out-of-plane Ni-O-Ni bond

angles obtained from single crystal structural determination: straightening the Ni–O–Ni angle lowers the transition temperature.

## 1. INTRODUCTION

Quasi-two-dimensional transition metal oxides with strong electron correlations have attracted much attention due to their collective properties such as high-temperature superconductivity in cuprates [1-5], colossal magnetoresistance in manganites [6], and metal-insulator transitions in nickelates [7]. Ordering of charge, spin and orbital are important phenomena underlying these exotic physical properties [1-5,8]. In particular, charge order, or charge density wave, has been established as a ubiquitous instability of the underdoped cuprate superconductors [9]. Charge order has also been found in non-copper transition metal oxides containing mixed valence states, such as  $\text{Mn}^{3+}/\text{Mn}^{4+}$  [10],  $\text{Ni}^{2+}/\text{Ni}^{3+}$  [11],  $\text{Ni}^{1+}/\text{Ni}^{2+}$  [12],  $\text{Fe}^{2+}/\text{Fe}^{3+}$  [13], and  $\text{Co}^{2+}/\text{Co}^{3+}$  [14]. One notable characteristic of charge order in these systems is their insulating ground state, instead of the metallic state found in cuprates [8]. The metallic Ruddlesden-Popper trilayer nickelates,  $\text{R}_4\text{Ni}_3\text{O}_{10}$  (R=La, Pr and Nd), contain nominal  $\text{Ni}^{2+}/\text{Ni}^{3+}$ , and thus are potential charge-ordered materials [15]. More importantly, the average valence state is  $2.67+$ , which can be thought as 0.67 holes based on background of  $2+$ . Such a hole doping level, if mapped to the cuprates, would lie well into the overdoped regime, which is generally regarded as conventional Fermi liquid possessing no collective electronic order. However, recently Peng *et al* discovered charge order in an overdoped cuprate without nesting or pseudogap features [16]. It is thus intriguing to establish if the ground state of these metallic trilayer nickelates also express charge order.

The trilayer nickelates  $\text{R}_4\text{Ni}_3\text{O}_{10}$  (R=La, and Pr) were reported by different research groups to undergo metal-to-metal transitions (MMTs,  $\sim 140$  K for  $\text{La}_4\text{Ni}_3\text{O}_{10}$  and  $\sim 160$  K for  $\text{Pr}_4\text{Ni}_3\text{O}_{10}$ ) based on powder samples [17-22]. The transition was ascribed by Zhang and Greenblatt to charge-density-wave-driven instabilities [18]. Later, Seo *et al.* published one-electron, tight-binding band structure (at the extended Hückel level), predicting a charge-density-wave nesting vector of  $q=0.3a^*$  or  $0.3b^*$  [23,24]. Direct evidence of charge-density-wave formation, *e.g.*, the observation of superlattice lines by x-ray, neutron or electron diffraction, has not been reported in the polycrystalline samples [18,21,25]. An obvious solution is study of single crystals. However, a challenge to crystal growth originates from the fact that  $\text{La}_4\text{Ni}_3\text{O}_{10}$  decomposes to  $\text{La}_3\text{Ni}_2\text{O}_7$  and NiO before it melts, as can be seen from the La-Ni-O phase diagram in Ref. [26].

Even the crystal structures of  $R_4Ni_3O_{10}$  ( $R=La, Pr, \text{ and } Nd$ ) above their MMTs are open questions. Based on Rietveld refinements on powder diffraction data, three different space groups have been proposed: (i) *Bmab* (or *Cmca*), as reported by Tkalich *et al* [17], Ling *et al* [21], and V.I. Voronin *et al* [27]. This structure consists of two La, two Ni and five O atoms in the asymmetric unit. (ii) *Imm2*. Zhang *et al.* reported *Fmmm* from powder x-ray diffraction, but their electron diffraction patterns show that the space group symmetry is lower than *F* or *C*, and the highest symmetry space group possible is *Imm2* [18]. (iii) *P2<sub>1</sub>/a*. Olafsen *et al.* reported *P2<sub>1</sub>/a* for  $Nd_4Ni_3O_{9.85}$  based on refinement of high-resolution powder synchrotron x-ray and neutron diffraction data [28]. Later, Nagell *et al.* refined their powder neutron diffraction data of  $La_4(Co_{1-x}Ni_x)_3O_{10+\delta}$  ( $0 \leq x \leq 1$ ) using this space group [29]. In this setting, the structure is composed of four La, four Ni and ten O atoms in the asymmetric unit. Notably, significant peak broadening from the anisotropic strain and stacking faults complicates determination of the crystal structure from powder diffraction refinements [29,30].

The outline of the paper is as follows. First we present the successful growth of bulk single crystals of  $R_4Ni_3O_{10}$  ( $R=La$  and  $Pr$ ) using the high-pressure optical-image floating zone technique. The obtained stable phases with increasing  $pO_2$  follows along the progression with  $n$  in  $La_{n+1}Ni_nO_{3n+1}$ . Next, we examine the heat capacity of both  $La_4Ni_3O_{10}$  and  $Pr_4Ni_3O_{10}$ , and report an unexpected phase transition at 147.5 K in  $La_4Ni_3O_{10}$  in addition to the 138.6 K transition reported in literature. Then we focus on the crystallographic structures above the MMTs by combining high-resolution x-ray powder diffraction, high-resolution neutron powder diffraction, and x-ray single crystal diffraction techniques. We find the as-grown  $La_4Ni_3O_{10}$  crystallizes in the *Bmab* space group with  $a=5.4163(13)$  Å,  $b=5.4687(12)$  Å,  $c=27.960(6)$  Å, or in *P2<sub>1</sub>/a* with  $a=5.4268(2)$  Å,  $b=5.4750(2)$  Å,  $c=27.9807(11)$  Å,  $\beta=90.116(1)^\circ$ , or a mixture of them, depending on the postgrowth cooling conditions, while the as-grown  $Pr_4Ni_3O_{10}$  belongs to *P2<sub>1</sub>/a* with  $a=5.3792(1)$  Å,  $b=5.4685(1)$  Å,  $c=27.5543(6)$  Å, and  $\beta=90.419(2)^\circ$ . The temperature dependent lattice parameters of  $R_4Ni_3O_{10}$  ( $R=La, Pr$ ) exhibit anomalies around the corresponding MMTs. The MMT temperatures correlate with the in-plane and out-of-plane Ni-O-Ni bond angles: deviating the Ni-O-Ni angle from  $180^\circ$  increases the transition temperature. Lastly we discuss the phase transition from *Bmab* to *P2<sub>1</sub>/a* by annealing the mixed phases of  $La_4Ni_3O_{10}$  in oxygen atmosphere. Finally we summarize our work in the concluding section.

## 2. EXPERIMENTAL SECTION

**2.1 Solid-State Reaction.** Precursors for crystal growth were synthesized via standard solid-state reaction techniques. Stoichiometric amounts of  $\text{La}_2\text{O}_3$  (Alfa Aesar, 99.99%) or  $\text{Pr}_6\text{O}_{11}$  (Alfa Aesar, 99.99%) and NiO (Alfa Aesar, 99.99%) were thoroughly ground. For  $\text{Pr}_4\text{Ni}_3\text{O}_{10}$ , an excess of 0.5-1.5% NiO was added to compensate the loss during growth due to volatilization during growth at high  $p\text{O}_2$  [31]. The mixture was then loaded into a Pt crucible and heated in air from room temperature to 1050 °C at a rate of 3 °C/min, allowed to dwell for 24 h, then furnace-cooled to room temperature. The solid was then reground, and sintered twice at 1050 °C using the procedures mentioned above. Powder x-ray diffraction showed mixed phases consisting of  $\text{La}_4\text{Ni}_3\text{O}_{10}$ ,  $\text{La}_3\text{Ni}_2\text{O}_7$ ,  $\text{La}_2\text{NiO}_4$ ,  $\text{La}_2\text{O}_3$  and NiO (see Figure S1).

**2.2 High- $p\text{O}_2$  Single Crystal Growth.** Single crystals of  $\text{R}_4\text{Ni}_3\text{O}_{10}$  (R=La, Pr) were successfully grown using a vertical optical-image floating-zone furnace designed for operation at elevated gas pressure (150 bar Model HKZ, SciDre GmbH, Dresden). Precursor powders of  $\text{La}_4\text{Ni}_3\text{O}_{10}$  were hydrostatically pressed into polycrystalline rods (length=100 mm, diameter=8 mm) and sintered for 24 h at 1400 °C to make a dense rod.  $\text{La}_4\text{Ni}_3\text{O}_{10}$  crystals were grown directly from the sintered rod at  $p\text{O}_2 = 20$  bar using a 3 kW Xenon arc lamp to heat the zone. A similar procedure was applied to  $\text{Pr}_4\text{Ni}_3\text{O}_{10}$  but severe cracking in the feed rod during growth resulted in melt zone loss. By reducing the sintering temperature to 1100 °C and making a less dense rod, the cracking issue was avoided.  $\text{Pr}_4\text{Ni}_3\text{O}_{10}$  crystals were grown at  $p\text{O}_2 = 140$  bar through two steps using a 5 kW Xenon arc lamp. The first step was a fast pass (30-50 mm/h) to improve density. This was followed by a second growth at the same pressure with slow travelling rate, 5 mm/h. During growth, a flow rate of 0.1 L/min of oxygen was maintained. Feed and seed rods were counter-rotated at 27 rpm and 20 rpm, respectively, to improve zone homogeneity.

**2.3 Single-Crystal Structural Determination.** Single crystal x-ray diffraction data were collected with a Bruker APEX2 area detector using lab x-ray at room temperature ( $\lambda=0.71073$  Å), and using synchrotron radiation ( $\lambda=0.41328$  Å) at 200 K at Beamline 15-ID-B at the Advanced Photon Source, Argonne National Laboratory. Single crystals with dimensions of approximately 40  $\mu\text{m}$  (lab) and 5  $\mu\text{m}$  (synchrotron) on an edge were mounted to the tip of glass fibers and collected using a Bruker D8 diffractometer. Indexing was performed using Bruker APEX2 software [32]. Data integration and cell refinement were performed using SAINT, and multi-scan absorption corrections were applied using the SADABS program [32]. The structure was solved by direct

methods and refined with full matrix least-squares methods on  $F^2$ . All atoms except oxygen were modeled using anisotropic ADPs, and the refinements converged for  $I > 2\sigma(I)$ . Calculations were performed using the SHELXTL crystallographic software package [33]. Details of crystal parameters, data collection and structure refinement for lab x-ray data are summarized in Table I.

Table I. Crystallographic data for  $R_4Ni_3O_{10}$  (R=La, Pr) above the metal-to-metal transition temperatures

Empirical formula	La <sub>4</sub> Ni <sub>3</sub> O <sub>10</sub>	La <sub>4</sub> Ni <sub>3</sub> O <sub>10</sub>	Pr <sub>4</sub> Ni <sub>3</sub> O <sub>10</sub>
Crystal system	orthorhombic	monoclinic	monoclinic
Space group	<i>Bmab</i>	<i>P2<sub>1</sub>/a</i>	<i>P2<sub>1</sub>/a</i>
Temperature, K	298(2)	200(2)	298(2)
Formula weight	891.77	891.77	899.77
<i>a</i> (Å)	5.4163(13)	5.4268(2)	5.3792(1)
<i>b</i> (Å)	5.4687(12)	5.4750(2)	5.4685(1)
<i>c</i> (Å)	27.960(6)	27.9807(11)	27.5543(6)
$\beta$ (°)	90	90.116(1)	90.419(2)
<i>V</i> (Å <sup>3</sup> )	828.2(3)	831.35(5)	810.52(3)
Density (calculated), g/cm <sup>3</sup>	7.152	7.125	7.374
<i>Z</i>	4	4	4
Radiation type	Synchrotron x-ray, 0.41328 Å	Synchrotron x-ray, 0.41328 Å	Mo K $\alpha$ , 0.71073 Å
Absorption coefficient, mm <sup>-1</sup>	5.633	5.612	30.418
Data collection Diffractometer	15-ID-B, APS	15-ID-B, APS	Bruker APEX2
Absorption correction	Multi-Scan	Multi-Scan	Multi-Scan
Reflections collected	4033	52038	21297
Independent reflections	821 ( $R_{int} = 0.0612$ )	4455 ( $R_{int} = 0.1048$ )	3867 ( $R_{int} = 0.0507$ )
$\theta$ range for data collection, °	0.847 to 18.383	0.846 to 20.865	1.478 to 36.318
F(000)	1568	1568	1600
Index ranges	-8 ≤ <i>h</i> ≤ 8, -8 ≤ <i>k</i> ≤ 7, -36 ≤ <i>l</i> ≤ 42	-9 ≤ <i>h</i> ≤ 9, -6 ≤ <i>k</i> ≤ 9, -48 ≤ <i>l</i> ≤ 39	-8 ≤ <i>h</i> ≤ 8, -8 ≤ <i>k</i> ≤ 9, -45 ≤ <i>l</i> ≤ 45
Refinement method	Full-matrix least-squares on $F^2$	Full-matrix least-squares on $F^2$	Full-matrix least-squares on $F^2$
Data / restraints / parameters	821 / 0 / 35	4455 / 0 / 105	3867 / 0 / 105
Goodness-of-fit	1.049	1.072	1.068
$R_1/wR_2$ ( $I > 2\sigma$ )	0.0520/0.1464	0.0739/0.2115	0.0533/0.1014
$R_1/wR_2$ (all)	0.1015/0.1927	0.1258/0.2401	0.0990/0.1183

$R = \sum ||F_o| - |F_c|| / \sum |F_o|$ ,  $wR = \{ \sum [w(|F_o|^2 - |F_c|^2)^2] / \sum [w(|F_o|^4)] \}^{1/2}$  and  $w = 1 / [\sigma^2(F_o^2) + (AP)^2 + BP]$  where  $P = (F_o^2 + 2Fc^2) / 3$ ,  $A = 0.1$ ,  $B = 0$  for La<sub>4</sub>Ni<sub>3</sub>O<sub>10</sub> with *Bmab*;  $A = 0.0658$ ,  $B = 171.8720$  for La<sub>4</sub>Ni<sub>3</sub>O<sub>10</sub> with *P2<sub>1</sub>/a*;  $A = 0.0174$ ,  $B = 72.3771$  for Pr<sub>4</sub>Ni<sub>3</sub>O<sub>10</sub> with *P2<sub>1</sub>/a*.

**2.4 Sample Annealing.** Under flowing oxygen, single crystals of  $\text{La}_4\text{Ni}_3\text{O}_{10}$  were heated to 1000 °C at a rate of 200 °C/h, held for 12 hours, and then cooled down to 200 °C at a rate of 30 °C/h, and finally to room temperature by turning off the furnace.

**2.5 Powder X-ray Diffraction (PXRD).** Room temperature PXRD was performed on a PANalytical X'Pert PRO diffractometer using  $\text{Cu K}\alpha$  radiation ( $\lambda=1.5418 \text{ \AA}$ ). High resolution PXRD data were collected at Beamline 11-BM in the range  $0.5^\circ \leq 2\theta \leq 28^\circ$  with a step size of  $0.001^\circ$  and counting time of 0.1 s per step and a wavelength of  $\lambda=0.459003 \text{ \AA}$  for  $\text{Pr}_4\text{Ni}_3\text{O}_{10}$  and  $\lambda=0.414579 \text{ \AA}$  for  $\text{La}_4\text{Ni}_3\text{O}_{10}$ . Samples were prepared by loading pulverized crystals into a  $\Phi 0.8$  mm Kapton capillary that was spun continuously at 5600 rpm during data collection. Diffraction patterns were recorded at room temperature first (1 h scan) and then on cooling from 296 to 100 K (10 min per scan, cooling rate of 0.3 K per min). An Oxford Cryostream 700 Plus  $\text{N}_2$  gas blower was used to control temperature. The same sample of  $\text{La}_4\text{Ni}_3\text{O}_{10}$  before and after annealing in flowing oxygen were measured at room temperature in the range  $0.5^\circ \leq 2\theta \leq 50^\circ$  with a step size of  $0.001^\circ$  and counting time of 0.1 s per step and a wavelength of  $\lambda=0.414167 \text{ \AA}$ . Data were analyzed with the Rietveld method using the GSAS-II software [34]. The background at each temperature was fit using Chebyshev polynomial (12-14 terms). Refined parameters include scale factor, phase ratio, lattice parameters, atomic positions, isotropic atomic displacement parameters (all La are grouped together, the same applies to Ni and O), and profile shape parameters. Isotropic domain size and generalized Mustrain models were used.

**2.6 Neutron Powder Diffraction (NPD).** Room temperature NPD data were collected on a time-of-flight (TOF) Super High Resolution Powder Diffractometer, Super HRPD [35,36] at the Material and Life science Facility (MLF) in the Japan Proton Accelerator Research Complex (J-PARC). The powder sample was installed in a cylindrical vanadium cell of dimensions 6 mm in diameter, 55 mm in height, and 100  $\mu\text{m}$  in thickness. All diffraction data were collected using all detectors in the range  $10^\circ < 2\theta < 172^\circ$ . The diffraction data from the Back-Scattering bank ( $15^\circ < 2\theta < 172^\circ$ ) were used for the analysis. Structural refinements were performed using Z-Rietveld software [37,38].

**2.7 Oxygen Content.** Oxygen contents of  $\text{R}_4\text{Ni}_3\text{O}_{10}$  (R=La, Pr) were determined by reduction in a 4%  $\text{H}_2/\text{N}_2$  mixture on a thermogravimetric analysis (Mettler Toledo Model TGA/DSC 1). Powder samples (~100 mg) were placed into a 150  $\mu\text{L}$   $\text{Al}_2\text{O}_3$  crucible and heated at a rate of 10 °C/min from room temperature to 900 °C, held for 5



hours, and then cooled at 10 °C/min to room temperature. Multiple blanks had been run previously to establish stability and buoyancy correction.

**2.8 Heat Capacity.** Heat capacity measurements were performed on a Quantum Design PPMS in the temperature range of 1.8-300 K. Apiezon-N vacuum grease was employed to fix crystals to the sapphire sample platform. The specific heat contribution from sample holder platform and grease was determined before mounting sample and subtracted from the total heat capacity.

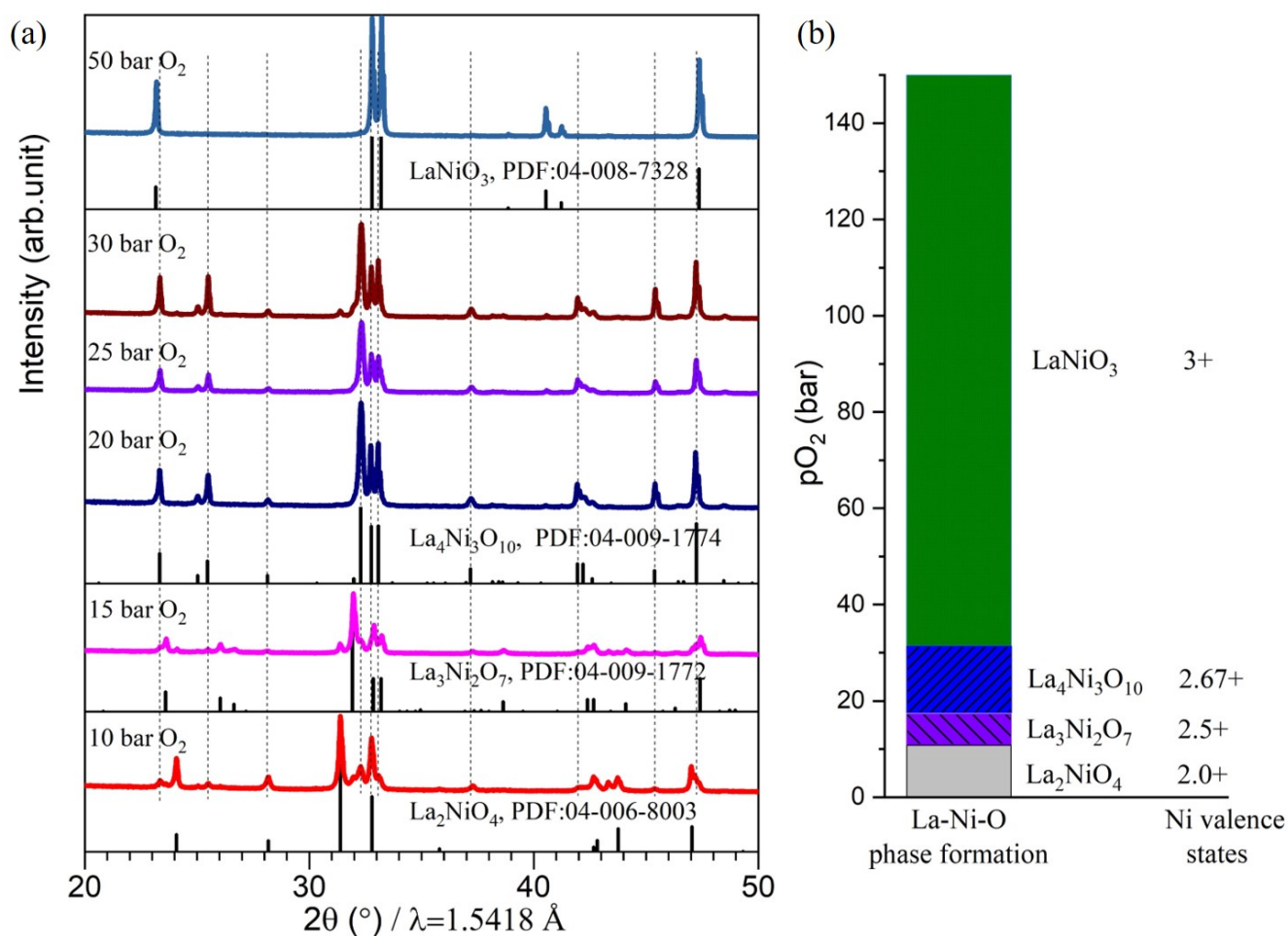


**Fig. 1** Melt quenching product of La<sub>2</sub>O<sub>3</sub>: NiO=2: 3 at various oxygen pressure. (a) Powder x-ray diffraction patterns vs pO<sub>2</sub> with standard patterns of La<sub>n+1</sub>Ni<sub>n</sub>O<sub>3n+1</sub> ( $n=1, 2, 3,$  and  $\infty$ ) from database shown as tick marks below the data; (b) Schematic drawing of La-Ni-O phase predominance as a function of pO<sub>2</sub>.

### 3. RESULTS AND DISCUSSION

**High pO<sub>2</sub> Crystal Growth.** We first explored phase formation as a function of oxygen pressure by melting and quenching materials with a starting composition of La:Ni=4:3 (see Figure S1). At pO<sub>2</sub>= 0.21 bar O<sub>2</sub>, La<sub>4</sub>Ni<sub>3</sub>O<sub>10</sub>

decomposes to  $\text{La}_3\text{Ni}_2\text{O}_7$ ,  $\text{NiO}$  and  $\text{O}_2$  at  $\sim 1400$  K based on the phase diagram reported by Zinkevich and Aldinger [22,26]. The lack of a tie line to a liquid phase precludes growth of a single crystal from the melt at ambient pressure. Considering the high valence state of Ni (nominal +2.67), a highly oxidizing environment is expected to help stabilize the target phase. Figure 1 presents the lab x-ray diffraction patterns of the phases obtained by quenching the melt at various  $p\text{O}_2$  with  $\text{La}_2\text{NiO}_4$ ,  $\text{La}_3\text{Ni}_2\text{O}_7$ ,  $\text{La}_4\text{Ni}_3\text{O}_{10}$  and  $\text{LaNiO}_3$  as references. Apparently, high  $p\text{O}_2$  is crucial for the formation of various Ruddlesden-Popper nickelates, and the stable phases with increasing pressure follows along the progression with  $n$  in  $\text{La}_{n+1}\text{Ni}_n\text{O}_{3n+1}$ , *i.e.*,  $\text{La}_2\text{NiO}_4$  was obtained at low  $p\text{O}_2$ ,  $\text{La}_3\text{Ni}_2\text{O}_7$  was the majority phase at  $\sim 14$  bar,  $\text{La}_4\text{Ni}_3\text{O}_{10}$  was obtained when  $p\text{O}_2$  is in the range of 16-30 bar (see Figure S2 at 20 bar  $\text{O}_2$ ), and  $\text{LaNiO}_3$  was the major phase at 50 bar. Figure 1b schematically illustrates the oxygen pressure stability range for different phases. More naturally, this is in line with Ni valence states. We have successfully grown metallic  $\text{LaNiO}_{3-\delta}$  at 40 and 130 bar  $\text{O}_2$  [39,40], as has Guo *et al* [41]. To optimize the  $p\text{O}_2$  for  $\text{R}_4\text{Ni}_3\text{O}_{10}$  (R=La and Pr) crystal growth, it is critical to use as high  $p\text{O}_2$  as possible to suppress the formation of single-layer  $\text{R}_2\text{NiO}_4$  and bilayer  $\text{R}_3\text{Ni}_2\text{O}_7$ , but also not too high to form perovskite phases  $\text{RNiO}_3$ . We found trace of  $\text{LaNiO}_3$  at  $p\text{O}_2 = 25$  bar for  $\text{La}_4\text{Ni}_3\text{O}_{10}$  growth in lab x-ray powder diffraction patterns, thus we adopted 20 bar  $p\text{O}_2$  for crystal growth of  $\text{La}_4\text{Ni}_3\text{O}_{10}$ . The same procedure was applied to the case of Pr-Ni-O, and we found  $\text{Pr}_2\text{NiO}_4$  formed at low pressure and  $\text{Pr}_4\text{Ni}_3\text{O}_{10}$  above 100 bar  $\text{O}_2$ . We were unable to stabilize either the bilayer  $\text{Pr}_3\text{Ni}_2\text{O}_7$  or the perovskite  $\text{PrNiO}_3$ . The missing  $\text{Pr}_3\text{Ni}_2\text{O}_7$  may reflect a very narrow pressure region of stability, and the missing  $\text{PrNiO}_3$  is because its formation requires  $p\text{O}_2$  higher than 150 bar. For the crystal growth of  $\text{Pr}_4\text{Ni}_3\text{O}_{10}$ , we employed oxygen pressure of 140 bar.

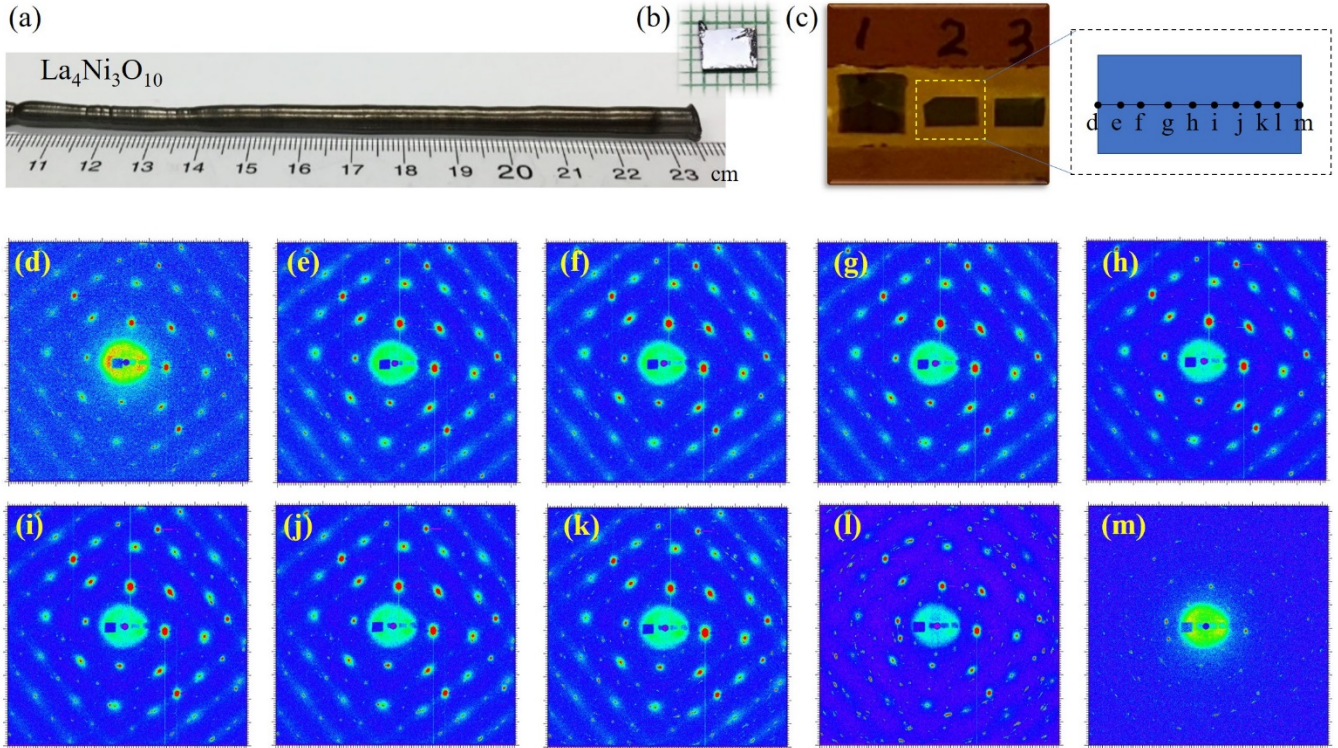


**Fig. 2**  $\text{La}_4\text{Ni}_3\text{O}_{10}$  single crystal and synchrotron x-ray diffraction. (a) Photograph of as-grown boule, (b) a cleaved  $\text{La}_4\text{Ni}_3\text{O}_{10}$  crystal, (c) a  $\text{La}_4\text{Ni}_3\text{O}_{10}$  crystal with  $\sim 4.5$  mm in length attached on Kapton tape and its diffraction pattern at various positions (d-m) (11-ID-C, APS).

To obtain high-quality single crystals of  $\text{R}_4\text{Ni}_3\text{O}_{10}$  ( $\text{R}=\text{La}$  and  $\text{Pr}$ ), we also investigated other growth parameters including traveling rates, feeding rates, and rotation speeds. We found that fast travelling rates, e.g., 30-50 mm/h, introduce second phases (e.g.,  $\text{La}_2\text{NiO}_4$ ) during growth, consistent with reports of disordered intergrowths of different  $n$  members of Ruddlesden-Popper phases [18]. Traveling rates of 4-6 mm/h for the seed were found to be acceptable. The rotation speeds of feed rod and seed are related to the growth interface between solid and liquid, and a planar or slightly convex interface shape with respect to the growth crystal is reported to be desirable [42]. As demonstrated in Ref. [43] for floating zone growth of  $\text{Y}_2\text{Ti}_2\text{O}_7$ , the shape of the growth interface changes from convex to less convex, and finally to concave with the speed of rotation of the crystals decreasing from 30 to 7 rpm. In our crystal growth, we applied rotation speeds of 27 and 20 rpm for feeding rod and seed, respectively, to achieve a stable melt zone and a convex growth front. A typical boule of  $\text{La}_4\text{Ni}_3\text{O}_{10}$  is shown in Figure 2a. Crystals with shiny facets were cleaved from the as-grown boule, as shown in Figure 2b. Figure 2c shows a cleaved  $\text{La}_4\text{Ni}_3\text{O}_{10}$  crystal,  $\sim 4.5$  mm in length. Diffraction patterns at various positions along the length of this

crystal using synchrotron x-rays at 11-ID-C, Advanced Photon Source are shown in Figures 2d-m. The observation of the same diffraction pattern from position  $d$  to  $l$  indicates a large single crystal with good crystallinity. The oxygen content of as-grown  $\text{La}_4\text{Ni}_3\text{O}_{10}$  and  $\text{Pr}_4\text{Ni}_3\text{O}_{10}$  were measured to be 9.98(1) and 10.05(1), respectively. Both as-grown  $\text{La}_4\text{Ni}_3\text{O}_{10}$  and  $\text{Pr}_4\text{Ni}_3\text{O}_{10}$  are essentially stoichiometric.

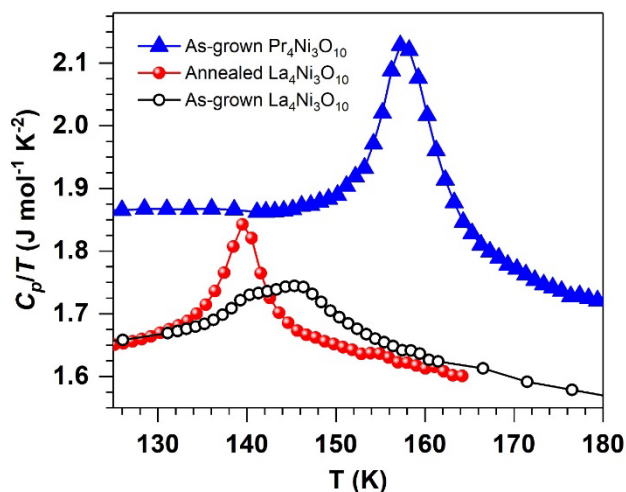


**Fig.3** Heat capacity of as-grown and annealed  $\text{La}_4\text{Ni}_3\text{O}_{10}$ , and as-grown  $\text{Pr}_4\text{Ni}_3\text{O}_{10}$ .

**Phase Behavior.** Lab x-ray powder diffraction shows that the pattern of pulverized as-grown crystals of  $\text{La}_4\text{Ni}_3\text{O}_{10}$  is consistent with previous reports [21,27], as can be seen from Figure 1 and Figure S2. To confirm the phase transition at  $\sim 140$  K in  $\text{La}_4\text{Ni}_3\text{O}_{10}$  [20,44] and  $\sim 160$  K in  $\text{Pr}_4\text{Ni}_3\text{O}_{10}$  [18,45] previously reported from polycrystalline samples, heat capacity measurements on single crystals were performed (see Figure 3). As expected, one anomaly at 157.6 K is observed in the  $C_p/T$  curve of as-grown  $\text{Pr}_4\text{Ni}_3\text{O}_{10}$ . Unexpectedly, two anomalies are observed in as-grown  $\text{La}_4\text{Ni}_3\text{O}_{10}$ , one at 138.6 K, which agrees with previous reports [20,44], and another at 147.5 K, which had not been reported. We consider two possibilities: (i) Two phases were obtained during crystal growth; (ii) A single phase was obtained during crystal growth, and it undergoes two subsequent phase transitions to its ground state. Arguing for the former explanation, Nagell *et al* reported that  $\text{La}_4\text{Ni}_3\text{O}_{10}$  transforms from tetragonal to orthorhombic at  $\sim 973$  K, and then to monoclinic at  $\sim 873$  K [30]. To understand the crystal structures, high resolution synchrotron x-ray and neutron powder diffraction experiments were carried out.



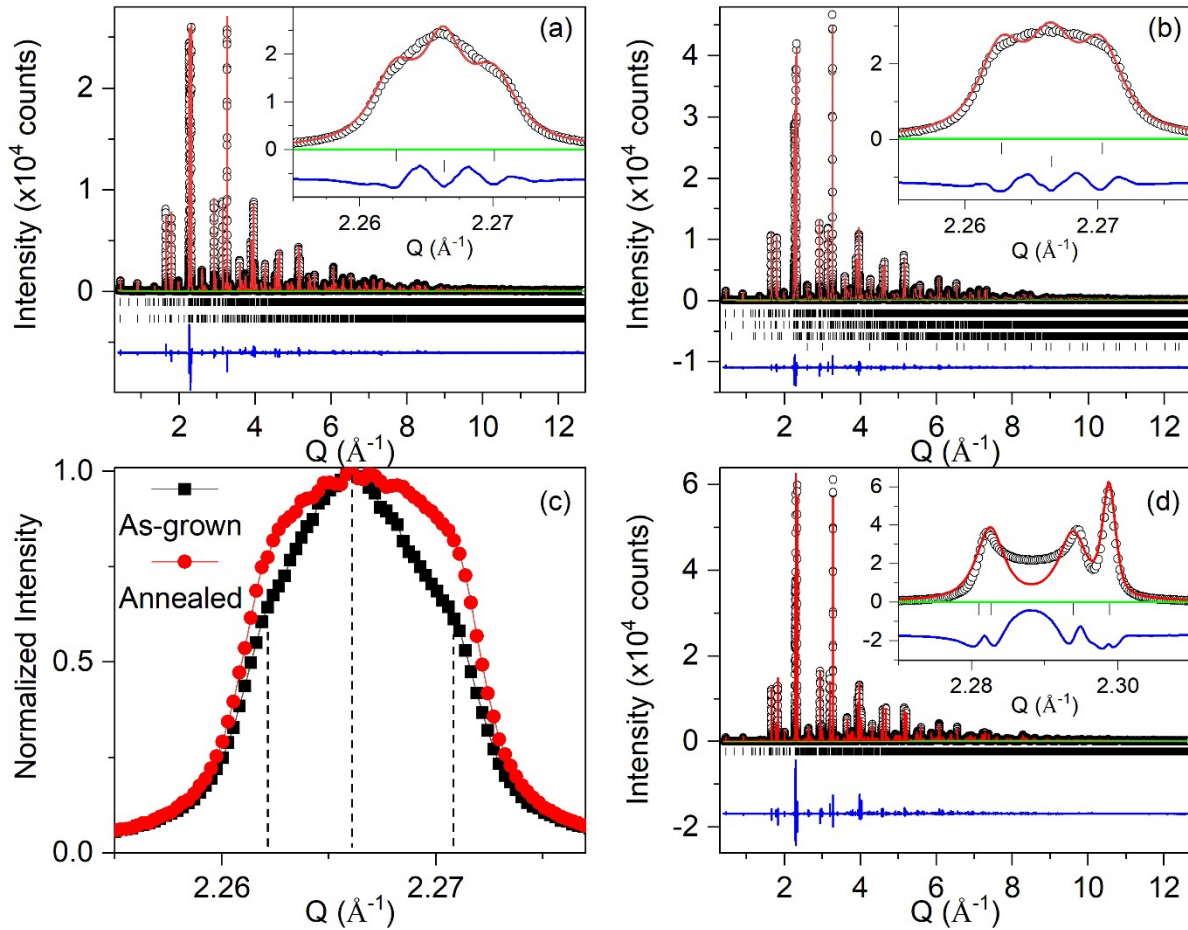


**Fig. 4** High-resolution synchrotron x-ray powder diffraction patterns of  $R_4Ni_3O_{10}$  ( $R=La$  and  $Pr$ ). (a) As-grown  $La_4Ni_3O_{10}$ . (b) Annealed  $La_4Ni_3O_{10}$ . (c) Comparison of as-grown and annealed  $La_4Ni_3O_{10}$  in the range of  $2.255 \leq Q \leq 2.277 \text{ \AA}^{-1}$ , where  $Q=4\pi\sin\theta/\lambda$ . (d) As-grown  $Pr_4Ni_3O_{10}$ . Black circle: observed data; red line: calculated intensity; green line: background; blue line: difference curve; black bars: Bragg peaks (a:  $P2_1/a$  for upper and  $Bmab$  for lower; b:  $P2_1/a$  for the first row,  $Bmab$  for the second row,  $La_3Ni_2O_7$  for the third row and  $NiO$  for the fourth row; d:  $P2_1/a$ ). Inserts show the quality of fit in  $Q$  range of  $2.255\sim 2.277 \text{ \AA}^{-1}$  for (a) and (b), and  $2.27\sim 2.31 \text{ \AA}^{-1}$  for (d).

**High-resolution synchrotron x-ray powder diffraction.** Figure 4a shows the high-resolution synchrotron x-ray powder diffraction pattern of as-grown  $La_4Ni_3O_{10}$  at room temperature and the Rietveld refinement using a two-phase  $Bmab$  and  $P2_1/a$  model obtained from single crystal x-ray diffraction (see below [Synchrotron X-ray Single Crystal Diffraction](#)) as a starting point. The refinement converged to  $R_{wp}=11.9\%$  and  $GOF=1.78$ . The obtained lattice parameters are  $a=5.4191(1) \text{ \AA}$ ,  $b=5.4721(1) \text{ \AA}$ ,  $c=27.9654(1) \text{ \AA}$  for  $Bmab$ , and  $a=5.4193(1) \text{ \AA}$ ,  $b=5.4717(1)$

$\text{\AA}$ ,  $c=27.9646(1) \text{\AA}$  and  $\beta=90.263(1)^\circ$  for  $P2_1/a$ . The inset of Figure 4a shows the pattern and fit in the  $Q$  range of  $2.255\sim 2.277 \text{\AA}^{-1}$ , where one can see clearly three peaks with two outer peaks from  $P2_1/a$  and an inner one from  $Bmab$ . Notably, the monoclinic distortion is subtle, and lab x-ray diffraction cannot resolve it (see Figure S2 and S3). In contrast, as-grown  $\text{Pr}_4\text{Ni}_3\text{O}_{10}$  crystallizes in the monoclinic  $P2_1/a$  space group with the fit converged to  $R_{wp}=20.3\%$  and  $\text{GOF}=4.08$  (see Figure 4d). The obtained lattice parameters are  $a=5.3776(1) \text{\AA}$ ,  $b=5.4671(1) \text{\AA}$ ,  $c=27.5506(1) \text{\AA}$  and  $\beta=90.388(1)^\circ$ . Some intensity is observed at  $Q\sim 2.29 \text{\AA}^{-1}$ , which may arise from stacking faults as reported previously [29,30].

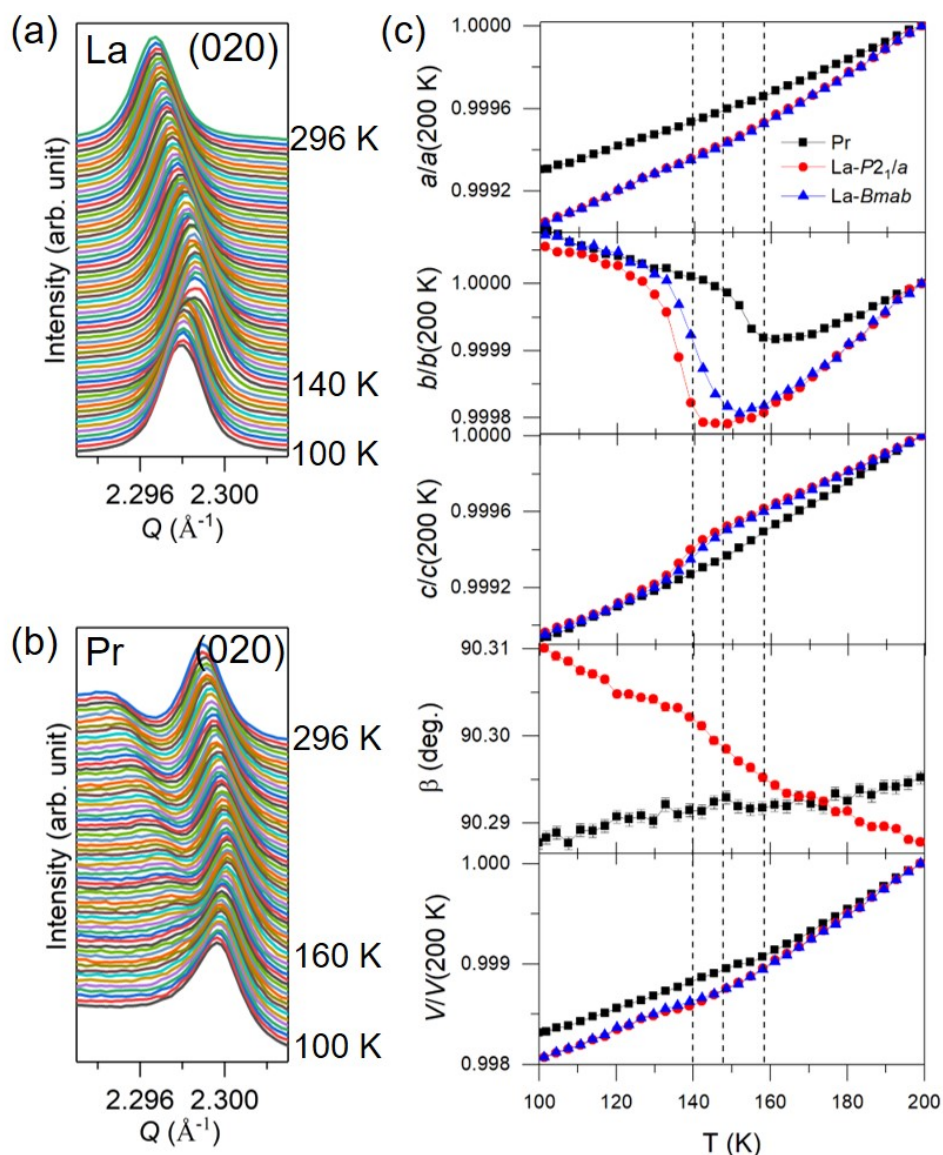


**Fig. 5** Temperature dependence of high-resolution synchrotron powder x-ray diffraction patterns of  $\text{R}_4\text{Ni}_3\text{O}_{10}$  ( $\text{R}=\text{La}$  and  $\text{Pr}$ ) and lattice parameters. (a) Evolution of the (020) peak of  $\text{La}_4\text{Ni}_3\text{O}_{10}$ . (b) Evolution of the (020) peak of  $\text{Pr}_4\text{Ni}_3\text{O}_{10}$ . (c) Lattice parameters ( $a$ ,  $b$ ,  $c$ ,  $\beta$ ,  $V$ ) as a function of temperature.

Figures 5a and b show the evolution of the (020) peak as a function of temperature for  $R_4Ni_3O_{10}$  ( $R=La$  and  $Pr$ ). The shift of the peak towards higher  $Q$  on cooling indicates contraction of  $b$  axis. No peak splitting or extra peaks were observed in the powder data through the MMTs. The  $La_4Ni_3O_{10}$  sample is a mixture of  $Bmab$ - and  $P2_1/a$  phases, and the data were refined using both phases. Figure 5c presents the temperature dependence of the unit cell parameters  $a$ ,  $b$ ,  $c$ ,  $\beta$ , and  $V$  (normalized to data at 200 K) in the range of 100-200 K extracted from Rietveld refinements. Anomalies are identified in the temperature dependence of lattice parameters, in particular in the  $b$  axis, reflecting a lattice contribution to the MMTs identified in the heat capacity measurement. Such a subtle lattice response,  $\sim 0.02\%$ , was missed previously [17,21].

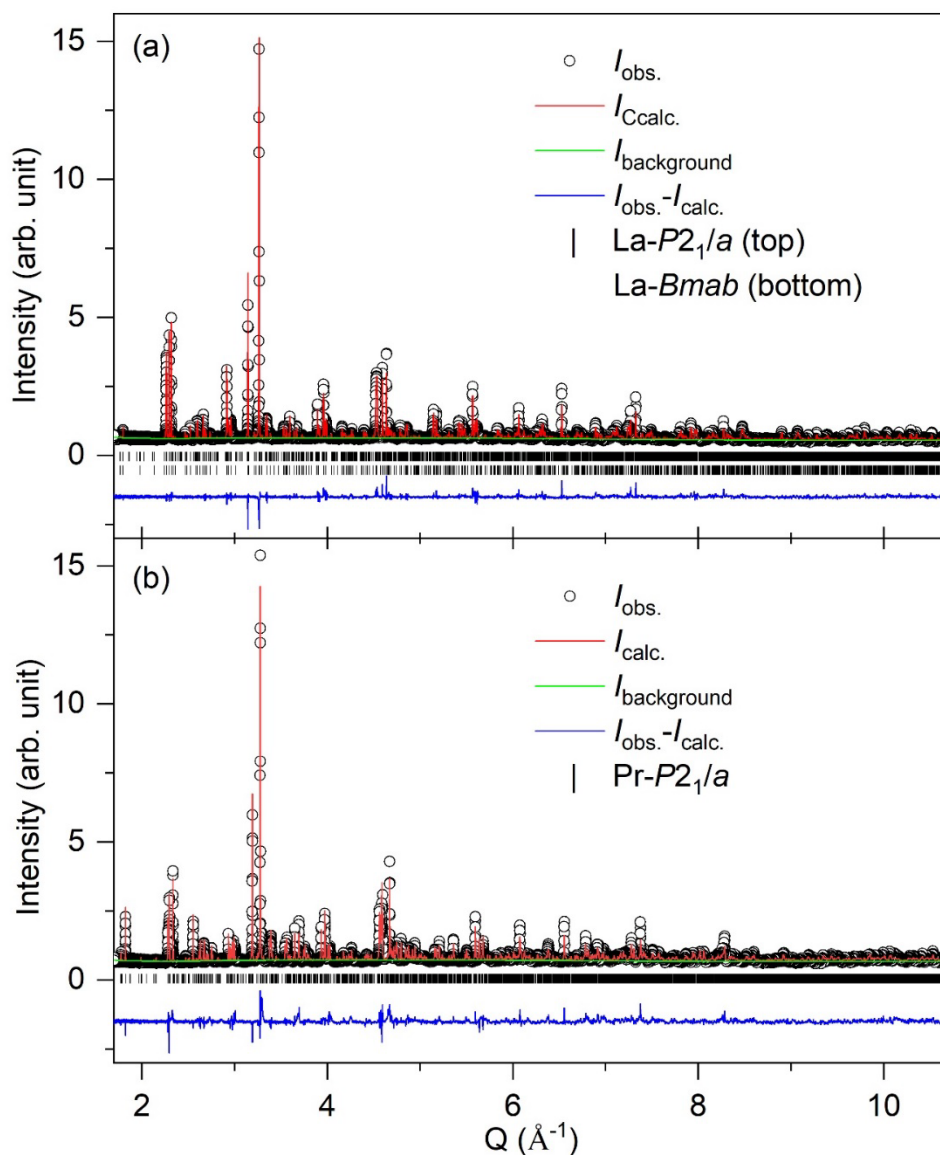


**Fig. 6** High-resolution time-of-flight neutron powder diffraction patterns of  $R_4Ni_3O_{10}$  ( $R=La$  and  $Pr$ ) at room temperature. (a)  $La_4Ni_3O_{10}$  (b)  $Pr_4Ni_3O_{10}$ .





**X-ray Single Crystal Diffraction.** Based on heat capacity, synchrotron x-ray, and neutron powder diffraction measurements of as-grown  $\text{La}_4\text{Ni}_3\text{O}_{10}$  and  $\text{Pr}_4\text{Ni}_3\text{O}_{10}$ , we find that  $\text{La}_4\text{Ni}_3\text{O}_{10}$  crystallizes in the orthorhombic and monoclinic structure while  $\text{Pr}_4\text{Ni}_3\text{O}_{10}$  belongs to monoclinic structure. To verify the results of synchrotron x-ray and neutron powder diffraction, in particular space groups and atomic positions, x-ray single crystal diffraction experiments were carried out. The unit cell of all  $\text{La}_4\text{Ni}_3\text{O}_{10}$  and  $\text{Pr}_4\text{Ni}_3\text{O}_{10}$  consists of two Ni-O trilayer blocks and two La-O rock salt layers (see [Figure 7](#)). One interesting feature of the structures is that there is a large distortion along  $b$  axis (the intermediate axis).

*Bmab*- $\text{La}_4\text{Ni}_3\text{O}_{10}$ . The asymmetric unit is composed of two La, two Ni and five O atoms. The La atoms are coordinated with 9 or 12 oxygen atoms, with bond distances ranging from 2.367(13) to 3.023(16) Å. Both Ni atoms are in octahedral coordination of oxygen atoms. The Ni-O bond length for the outer Ni of the trilayer are in the range of 1.925(2)-2.188(13) Å, and the inner Ni 1.937(2)-1.954(14) Å. Bond valence calculations [46] reveal 2.9-3.0 for La, 2.7 for the outer layer Ni and 2.9 for the inner layer Ni, consistent with nominal oxidation states.

*P2<sub>1</sub>/a*- $\text{La}_4\text{Ni}_3\text{O}_{10}$  and  $\text{Pr}_4\text{Ni}_3\text{O}_{10}$ . The monoclinic structure of  $\text{La}_4\text{Ni}_3\text{O}_{10}$  belongs to the *P2<sub>1</sub>/a* space group. Among the *P2<sub>1</sub>/a* crystal structure reported previously, Olafsen *et al* [28] and Nagell *et al* [29,30] utilized a unit cell of  $a \sim 5.41$  Å,  $b \sim 5.46$  Å,  $c \sim 27.96$  Å and  $\beta \sim 90.2^\circ$ , while Puggioni and Rondinelli [47] reported  $a \sim 5.41$  Å,  $b \sim 5.46$  Å,  $c \sim 14.2$  Å and  $\beta \sim 100.9^\circ$ . Our unit cell setting is the same as Olafsen *et al* and Nagell *et al*, but the structural details are rather different. In our model obtained from single crystal x-ray diffraction, the asymmetric unit consists of four La, three Ni and ten O atoms, and the origin of the unit cell is shifted compared with Olafsen *et al* [28] and Nagell *et al* [29,30]. [Figures 7b-c](#) show the structures of *P2<sub>1</sub>/a*- $\text{La}_4\text{Ni}_3\text{O}_{10}$  and  $\text{Pr}_4\text{Ni}_3\text{O}_{10}$ . In the asymmetric unit, two La (Pr) atoms are in 9 coordination and the other two are in 12 coordination of oxygen atoms, all Ni atoms are surrounded by six oxygen atoms. The bond distances for La-O are in the range of 2.367(11)-3.014(13) Å in *P2<sub>1</sub>/c*- $\text{La}_4\text{Ni}_3\text{O}_{10}$ . In contrast, the shortest bond length for Pr-O is 2.328(11) Å in  $\text{Pr}_4\text{Ni}_3\text{O}_{10}$ . The outer Ni atoms of the trilayer are strongly distorted compared with the inner Ni, with bond distances of 1.912(12)-2.199(11) Å (outer) and 1.920(13)-1.955(16) Å (inner) for *P2<sub>1</sub>/a*- $\text{La}_4\text{Ni}_3\text{O}_{10}$ , and 1.911(12)-2.174(11) Å (outer) and 1.915(11)-1.967(12) Å (inner) for  $\text{Pr}_4\text{Ni}_3\text{O}_{10}$ . Bond valence calculations [46]

reveal 2.9-3.0 for La, 2.7 for the outer layer Ni and 3.0 for the inner layer Ni in  $P2_1/a$ - $\text{La}_4\text{Ni}_3\text{O}_{10}$ , and 2.7-3.0 for Pr, 2.7 for the outer layer Ni and 2.9 for the inner layer Ni in  $\text{Pr}_4\text{Ni}_3\text{O}_{10}$ . The calculated values for La and Pr are acceptably close to the corresponding expected values based on ionic charge.

Table II. In-plane and out-of-plane Ni-O-Ni angle (°)

Compound	$P2_1/a$ - $\text{La}_4\text{Ni}_3\text{O}_{10}$	$Bmab$ - $\text{La}_4\text{Ni}_3\text{O}_{10}$	$\text{Pr}_4\text{Ni}_3\text{O}_{10}$	$\text{Nd}_4\text{Ni}_3\text{O}_{10}$ [28]
In-plane	170.0(8), 172.1(8), 164.3(10), 168.3(12), 171.1(8), 170.5(8)	167.7(8), 166.9(10)	167.7(7), 164.8(7), 157.6(7), 156.3(7), 167.7(7), 165.0(7)	154(1), 161(1), 165(1), 161(1), 161(1), 168(1)
average	169.4	167.3	163.2	161.7
Out-of-plane	164.1(8), 164.3(8)	163.7(9)	158.1(7), 158.3(7)	157(1), 156(1)
average	164.2	163.7	158.2	156.5
Metal-to-metal transition (K)	138.6	147.5	157.6	165 [18]

The in-plane and out-of-plane Ni-O-Ni bond angles, as shown in Table II, correlate with the MMTs in  $\text{R}_4\text{Ni}_3\text{O}_{10}$  (R=La, Pr and Nd). As the average Ni-O-Ni angle deviates from 180°, the MMT temperature increases. A similar observation has been reported in the perovskite series  $\text{RNiO}_3$  (R=Pr-Lu) [48], where a sharp metal-insulator transition is mainly determined by the Ni-O-Ni bond angle.

**Phase Transformation from  $Bmab$  to  $P2_1/a$ .** The observation of the coexistence of  $Bmab$  and  $P2_1/a$  in the as-grown  $\text{La}_4\text{Ni}_3\text{O}_{10}$  and purely monoclinic  $P2_1/a$  in the as-grown  $\text{Pr}_4\text{Ni}_3\text{O}_{10}$  directed us to explore whether  $Bmab$  can transform to  $P2_1/a$  by annealing. We annealed the as-grown crystal by flowing oxygen at 1273 K to minimize the decomposition of  $\text{La}_4\text{Ni}_3\text{O}_{10}$ . The heat capacity of the as-grown and annealed crystal (the same sample) is presented in Figure 3. Clearly, the peak centered at 147.5 K disappears and the peak at 138.6 K becomes more pronounced, consistent with conversion from  $Bmab$  to  $P2_1/a$ . Additional evidence of the phase transition can be obtained from high-resolution synchrotron x-ray powder diffraction. Figure 4b shows the diffraction pattern of annealed  $\text{La}_4\text{Ni}_3\text{O}_{10}$ . After annealing, we observed the appearance of minor amounts of  $\text{La}_3\text{Ni}_2\text{O}_7$  and NiO ( $I/I_{\text{max}} < 1\%$ ), indicating slight decomposition of  $\text{La}_4\text{Ni}_3\text{O}_{10}$ . The refinement converged to  $R_{\text{wp}}=10.5\%$  and  $\text{GOF}=1.78$ . The obtained lattice parameters are  $a=5.4185(1)$  Å,  $b=5.4711(1)$  Å,  $c=27.9645(1)$  Å for  $Bmab$ - $\text{La}_4\text{Ni}_3\text{O}_{10}$ , and  $a=5.4186(1)$  Å,  $b=5.4711(1)$  Å,  $c=27.9649(1)$  Å and  $\beta=90.271(1)^\circ$  for  $P2_1/a$ - $\text{La}_4\text{Ni}_3\text{O}_{10}$ . The inset of Figure 4b shows the fit quality around  $Q \sim 2.265$  Å<sup>-1</sup>. Figure 4c presents the peak around  $Q \sim 2.265$  Å<sup>-1</sup> before

and after annealing in flowing oxygen by normalizing their heights. The intensity of the  $P2_1/a$  phase increased significantly after annealing, confirming the conversion from  $Bmab$  to  $P2_1/a$ . Our results agree with those of Nagell *et al* that  $\text{La}_4\text{Ni}_3\text{O}_{10}$  transforms from orthorhombic to monoclinic [30]. Such a conversion from  $Bmab$  to  $P2_1/a$  also occurs in  $\text{Pr}_4\text{Ni}_3\text{O}_{10}$ , as we obtained mixed phases by quenching the boule at 140 bar  $\text{O}_2$  (see Figure S5). By optimizing annealing conditions such as temperature, time and oxygen pressure (suppressing decomposition), a complete transformation from  $Bmab$  to  $P2_1/a$  may be possible in the La case.

#### 4. CONCLUSION

In summary, we successfully obtained single crystals of  $\text{La}_4\text{Ni}_3\text{O}_{10}$  with two different crystal structure ( $Bmab$  and  $P2_1/a$ ) and  $\text{Pr}_4\text{Ni}_3\text{O}_{10}$  ( $P2_1/a$ ) using a high pressure floating zone furnace. Crystal structures of  $\text{R}_4\text{Ni}_3\text{O}_{10}$  (R=La, Pr) were determined by combining synchrotron x-ray single crystal diffraction, high-resolution synchrotron x-ray and neutron powder diffraction. Temperature dependence of lattice parameters indicates structural response to their metal-to-metal transitions. Unambiguous evidence will be the observation of superlattice peaks from x-ray or neutron single crystal diffraction, and we will present them in a separate paper. The availability of these  $\text{R}_4\text{Ni}_3\text{O}_{10}$  (R=La, Pr) single crystals provides the opportunity to finally test the charge-density-wave theory.

#### AUTHOR INFORMATION

Corresponding Author

[\\*junjie.zhang.sdu@gmail.com](mailto:junjie.zhang.sdu@gmail.com), or [zhangj4@ornl.gov](mailto:zhangj4@ornl.gov)

#### ACKNOWLEDGMENTS

This work was supported by the US Department of Energy, Office of Science, Basic Energy Sciences, Materials Science and Engineering Division. NSF's ChemMatCARS Sector 15 is supported by the Divisions of Chemistry (CHE) and Materials Research (DMR), National Science Foundation, under grant number NSF/CHE-1834750. Use of the Advanced Photon Source, an Office of Science User Facility operated for the U.S. Department of Energy (DOE) Office of Science by Argonne National Laboratory, was supported by the U.S. DOE under Contract No. DE-AC02-06CH11357. This research has been supported in part by ORNL Postdoctoral

Development Fund by UT-Battelle, LLC under Contract No. DE-AC05-00OR22725 with the U.S. Department of Energy. J. Z. thanks Dr. Saul H. Lapidus for his help with the high-resolution powder diffraction experiment at 11-BM, and Drs. Raphael P. Hermann, D. Phelan, A. S. Botana, M. R. Norman, J. W. Freeland, V. Pardo, W. E. Pickett, and S. Rosenkranz for fruitful discussions.

## REFERENCES

- [1] M. R. Norman, Materials design for new superconductors. *Rep. Prog. Phys.* **79**, 074502 (2016).
- [2] J. M. Tranquada, Exploring intertwined orders in cuprate superconductors. *Physica B* **460**, 136 (2015).
- [3] A. A. Kordyuk, Pseudogap from ARPES experiment: three gaps in cuprates and topological superconductivity (Review Article). *Low Temp. Phys.* **41**, 319 (2015).
- [4] B. Keimer, S. A. Kivelson, M. R. Norman, S. Uchida, and J. Zaanen, From quantum matter to high-temperature superconductivity in copper oxides. *Nature* **518**, 179 (2015).
- [5] E. Fradkin, S. A. Kivelson, and J. M. Tranquada, Colloquium: Theory of intertwined orders in high temperature superconductors. *Rev. Mod. Phys.* **87**, 457 (2015).
- [6] M. B. Salamon and M. Jaime, The physics of manganites: Structure and transport. *Rev. Mod. Phys.* **73**, 583 (2001).
- [7] J. M. Tranquada, Spins, stripes, and superconductivity in hole-doped cuprates. *AIP Conf. Proc.* **1550**, 114 (2013).
- [8] H. Ulbrich and M. Braden, Neutron scattering studies on stripe phases in non-cuprate materials. *Physica C* **481**, 31 (2012).
- [9] H. Miao, J. Lorenzana, G. Seibold, Y. Y. Peng, A. Amorese, F. Yakhou-Harris, K. Kummer, N. B. Brookes, R. M. Konik, V. Thampy, G. D. Gu, G. Ghiringhelli, L. Braicovich, and M. P. M. Dean, High-temperature charge density wave correlations in  $\text{La}_{1.875}\text{Ba}_{0.125}\text{CuO}_4$  without spin-charge locking. *Proc. Natl. Acad. Sci. USA* **114**, 12430 (2017).
- [10] Z. Sun, Q. Wang, A. V. Fedorov, H. Zheng, J. F. Mitchell, and D. S. Dessau, Localization of electrons due to orbitally ordered bi-stripes in the bilayer manganite  $\text{La}_{2-2x}\text{Sr}_{1+2x}\text{Mn}_2\text{O}_7$  ( $x \sim 0.59$ ). *Proc. Natl. Acad. Sci. USA* **108**, 11799 (2011).

- [11] S. Anissimova, D. Parshall, G. D. Gu, K. Marty, M. D. Lumsden, S. Chi, J. A. Fernandez-Baca, D. L. Abernathy, D. Lamago, J. M. Tranquada, and D. Reznik, Direct observation of dynamic charge stripes in  $\text{La}_{2-x}\text{Sr}_x\text{NiO}_4$ . *Nat. Commun.* **5**, 3467 (2014).
- [12] J. Zhang, Y. S. Chen, D. Phelan, H. Zheng, M. R. Norman, and J. F. Mitchell, Stacked charge stripes in the quasi-2D trilayer nickelate  $\text{La}_4\text{Ni}_3\text{O}_8$ . *Proc. Natl. Acad. Sci. USA* **113**, 8945 (2016).
- [13] M. S. Senn, J. P. Wright, and J. P. Attfield, Charge order and three-site distortions in the Verwey structure of magnetite. *Nature* **481**, 173 (2011).
- [14] M. Cwik, M. Benomar, T. Finger, Y. Sidis, D. Senff, M. Reuther, T. Lorenz, and M. Braden, Magnetic correlations in  $\text{La}_{2-x}\text{Sr}_x\text{CoO}_4$  studied by neutron scattering: possible evidence for stripe phases. *Phys. Rev. Lett.* **102**, 057201 (2009).
- [15] M. Greenblatt, Ruddlesden-popper  $\text{Ln}_{n+1}\text{Ni}_n\text{O}_{3n+1}$  nickelates: Structure and properties. *Curr. Opin. Solid State Mater. Sci.* **2**, 174 (1997).
- [16] Y. Y. Peng, R. Fumagalli, Y. Ding, M. Minola, S. Caprara, D. Betto, M. Bluschke, G. M. De Luca, K. Kummer, E. Lefrançois, M. Salluzzo, H. Suzuki, M. Le Tacon, X. J. Zhou, N. B. Brookes, B. Keimer, L. Braicovich, M. Grilli, and G. Ghiringhelli, Re-entrant charge order in overdoped  $(\text{Bi,Pb})_{2.12}\text{Sr}_{1.88}\text{CuO}_{6+\delta}$  outside the pseudogap regime. *Nat. Mater.* **17**, 697 (2018).
- [17] A. K. Tkalich, V. P. Glazkov, V. A. Somenkov, S. S. Shil'shtein, A. E. Kar'kim, and A. V. Mirmel'shtein, Synthesis, structure, and properties of nickelates  $\text{R}_4\text{Ni}_3\text{O}_{10}$  ( $\text{R}=\text{Nd,Pr,La}$ ). *Superconductivity* **4**, 2280 (1991).
- [18] Z. Zhang and M. Greenblatt, Synthesis, structure, and properties of  $\text{Ln}_4\text{Ni}_3\text{O}_{10-\delta}$  ( $\text{Ln}=\text{La, Pr, and Nd}$ ). *J. Solid State Chem.* **117**, 236 (1995).
- [19] Y. Kobayashi, S. Taniguchi, M. Kasai, M. Sato, T. Nishioka, and M. Kontani, Transport and magnetic properties of  $\text{La}_3\text{Ni}_2\text{O}_{7-\delta}$  and  $\text{La}_4\text{Ni}_3\text{O}_{10-\delta}$ . *J. Phys. Soc. Jpn.* **65**, 3978 (1996).
- [20] M. D. Carvalho, M. M. Cruz, A. Wattiaux, J. M. Bassat, F. M. A. Costa, and M. Godinho, Influence of oxygen stoichiometry on the electronic properties of  $\text{La}_4\text{Ni}_3\text{O}_{10\pm\delta}$ . *J. Appl. Phys.* **88**, 544 (2000).
- [21] C. D. Ling, D. N. Argyriou, G. Wu, and J. J. Neumeier, Neutron diffraction study of  $\text{La}_3\text{Ni}_2\text{O}_7$ : structural relationships among  $n=1, 2$ , and 3 phases  $\text{La}_{n+1}\text{Ni}_n\text{O}_{3n+1}$ . *J. Solid State Chem.* **152**, 517 (2000).

- [22] M. Zinkevich, N. Solak, H. Nitsche, M. Ahrens, and F. Aldinger, Stability and thermodynamic functions of lanthanum nickelates. *J. Alloys Compd.* **438**, 92 (2007).
- [23] D. K. Seo, W. Liang, M. H. Whangbo, Z. Zhang, and M. Greenblatt, Electronic band structure and madelung potential study of the nickelates  $\text{La}_2\text{NiO}_4$ ,  $\text{La}_3\text{Ni}_2\text{O}_7$ , and  $\text{La}_4\text{Ni}_3\text{O}_{10}$ . *Inorg. Chem.* **35**, 6396 (1996).
- [24] M. Greenblatt, Z. Zhang, and M. H. Whangbo, Electronic properties of  $\text{La}_3\text{Ni}_2\text{O}_7$  and  $\text{Ln}_4\text{Ni}_3\text{O}_{10}$ , Ln=La, Pr and Nd. *Synth. Met.* **85**, 1451 (1997).
- [25] M. D. Carvalho, F. M. A. Costa, I. D. S. Pereira, A. Wattiaux, J. M. Bassat, J. C. Grenier, and M. Pouchard, New preparation method of  $\text{La}_{n+1}\text{Ni}_n\text{O}_{3n+1-\delta}$  ( $n = 2, 3$ ). *J. Mater. Chem.* **7**, 2107 (1997).
- [26] M. Zinkevich and F. Aldinger, Thermodynamic analysis of the ternary La-Ni-O system. *J. Alloys Compd.* **375**, 147 (2004).
- [27] V. I. Voronin, I. F. Berger, V. A. Cherepanov, L. Y. Gavrilova, A. N. Petrov, A. I. Ancharov, B. P. Tolochko, and S. G. Nikitenko, Neutron diffraction, synchrotron radiation and EXAFS spectroscopy study of crystal structure peculiarities of the lanthanum nickelates  $\text{La}_{n+1}\text{Ni}_n\text{O}_y$  ( $n=1,2,3$ ). *Nucl. Instrum. Meth. A.* **470**, 202 (2001).
- [28] A. Olafsen, H. Fjellvåg, and B. C. Hauback, Crystal Structure and Properties of  $\text{Nd}_4\text{Co}_3\text{O}_{10+\delta}$  and  $\text{Nd}_4\text{Ni}_3\text{O}_{10-\delta}$ . *J. Solid State Chem.* **151**, 46 (2000).
- [29] M. U. Nagell, S. Kumar, M. H. Sørby, H. Fjellvåg, and A. O. Sjøstad, Structural and magnetic aspects of  $\text{La}_4(\text{Co}_{1-x}\text{Ni}_x)_3\text{O}_{10+\delta}$  ( $0 \leq x \leq 1$ ). *Phase Transit.* **88**, 979 (2015).
- [30] M. U. Nagell, W. A. Sławiński, P. Vajeeston, H. Fjellvåg, and A. O. Sjøstad, Temperature induced transitions in  $\text{La}_4(\text{Co}_{1-x}\text{Ni}_x)_3\text{O}_{10+\delta}$ ; oxygen stoichiometry and mobility. *Solid State Ionics* **305**, 7 (2017).
- [31] W. A. Phelan, J. Zahn, Z. Kennedy, and T. M. McQueen, Pushing Boundaries: High Pressure, Supercritical Optical Floating Zone Materials Discovery. *J. Solid State Chem.* **270**, 705 (2018).
- [32] Bruker, APEX2, Bruker Analytical X-ray Instruments, Inc. Madison, Wisconsin, USA., 2014.
- [33] G. M. Sheldrick, computer code SHELXTL, Bruker Analytical X-ray Instruments, Inc. Madison, WI, 2001.
- [34] B. H. Toby and R. B. Von Dreele, GSAS-II: the genesis of a modern open-source all purpose crystallography software package. *J. Appl. Crystallogr.* **46**, 544 (2013).

- [35] S. Torii, M. Yonemura, Y. Ishikawa, P. Miao, R. Tomiyasu, S. Satoh, Y. Noda, and T. Kamiyama, Improvement of Instrument Devices for Super High Resolution Powder Diffractometer at J-PARC. *J. Phys.: Conf. Ser.* **502**, 012052 (2014).
- [36] S. Torii, M. Yonemura, T. Yulius Surya Panca Putra, J. Zhang, P. Miao, T. Muroya, R. Tomiyasu, T. Morishima, S. Sato, H. Sagehashi, Y. Noda, and T. Kamiyama, Super High Resolution Powder Diffractometer at J-PARC. *J. Phys. Soc. Jpn.* **80**, SB020 (2011).
- [37] R. Oishi, M. Yonemura, Y. Nishimaki, S. Torii, A. Hoshikawa, T. Ishigaki, T. Morishima, K. Mori, and T. Kamiyama, Rietveld analysis software for J-PARC. *Nucl. Instrum. Methods Phys. Res. A* **600**, 94 (2009).
- [38] R. Oishi-Tomiyasu, M. Yonemura, T. Morishima, A. Hoshikawa, S. Torii, T. Ishigaki, and T. Kamiyama, Application of matrix decomposition algorithms for singular matrices to the Pawley method in Z-Rietveld. *J. Appl. Crystallogr.* **45**, 299 (2012).
- [39] J. Zhang, H. Zheng, Y. Ren, and J. F. Mitchell, High-Pressure Floating-Zone Growth of Perovskite Nickelate  $\text{LaNiO}_3$  Single Crystals. *Cryst. Growth Des.* **17**, 2730 (2017).
- [40] B.-X. Wang, S. Rosenkranz, X. Rui, J. Zhang, F. Ye, H. Zheng, R. F. Klie, J. F. Mitchell, and D. Phelan, Antiferromagnetic defect structure in  $\text{LaNiO}_{3-\delta}$  single crystals. *Phys. Rev. Mater.* **2**, 064404 (2018).
- [41] H. Guo, Z. W. Li, L. Zhao, Z. Hu, C. F. Chang, C. Y. Kuo, W. Schmidt, A. Piovano, T. W. Pi, O. Sobolev, D. I. Khomskii, L. H. Tjeng, and A. C. Komarek, Antiferromagnetic correlations in the metallic strongly correlated transition metal oxide  $\text{LaNiO}_3$ . *Nat. Commun.* **9**, 43 (2018).
- [42] S. M. Koohpayeh, D. Fort, and J. S. Abell, The optical floating zone technique: A review of experimental procedures with special reference to oxides. *Prog. Cryst. Growth Charact. Mater.* **54**, 121 (2008).
- [43] C. Liu, A. Dabkowski, W.-Q. Jie, B. D. Gaulin, and H. A. Dabkowska, Optical observation of striations in  $\text{Y}_2\text{Ti}_2\text{O}_7$  single crystals. *Crystals* (2019).
- [44] G. Q. Wu, J. J. Neumeier, and M. F. Hundley, Magnetic susceptibility, heat capacity, and pressure dependence of the electrical resistivity of  $\text{La}_3\text{Ni}_2\text{O}_7$  and  $\text{La}_4\text{Ni}_3\text{O}_{10}$ . *Phys. Rev. B* **63**, 245120 (2001).
- [45] J. M. Bassat, C. Allançon, P. Odier, J. P. Loup, M. D. Carvalho, and A. Wattiaux, Electronic properties of  $\text{Pr}_4\text{Ni}_3\text{O}_{10\pm\delta}$ . *Eur. J. Solid State Inorg. Chem.* **35**, 173 (1998).

- [46] A. Altomare, C. Cuocci, C. Giacobazzo, A. Moliterni, R. Rizzi, N. Corriero, and A. Falcicchio, EXPO2013: a kit of tools for phasing crystal structures from powder data. *J. Appl. Crystallogr.* **46**, 1231 (2013).
- [47] D. Puggioni and J. M. Rondinelli, Crystal structure stability and electronic properties of the layered nickelate  $\text{La}_4\text{Ni}_3\text{O}_{10}$ . *Phys. Rev. B* **97**, 115116 (2018).
- [48] S. Catalano, M. Gibert, J. Fowlie, J. Íñiguez, J. M. Triscone, and J. Kreisel, Rare-earth nickelates  $\text{RNiO}_3$  : thin films and heterostructures. *Rep. Prog. Phys.* **81**, 046501 (2018).